



Wavelet-based spatiotemporal analyses of climate and vegetation for the Athabasca river basin in Canada

Hatef Dastour ^{a,1}, Ebrahim Ghaderpour ^{a,b,1,2}, Mohamed Sherif Zaghloul ^a, Babak Farjad ^c,
Anil Gupta ^{a,c}, Hyung Eum ^c, Gopal Achari ^d, Quazi K. Hassan ^{a,*}

^a Department of Geomatics Engineering, University of Calgary, 2500 University Drive NW, Calgary, AB T2N 1N4, Canada

^b Department of Earth Sciences, Sapienza University of Rome, Piazzale Aldo Moro, 5, 00185, Rome, Italy

^c Resource Stewardship Division, Alberta Environment and Parks, 3535 Research Road NW, University Research Park, Calgary, AB T2L 2K8, Canada

^d Department of Civil Engineering, University of Calgary, 2500 University Drive NW, Calgary, Alberta, Canada

ARTICLE INFO

Keywords:

MODIS
Trend analysis
Spectral analysis
Coherency analysis
Phase discrepancy
NDVI
Land Use/Land Cover

ABSTRACT

Monitoring spatiotemporal changes in climate and vegetation coverage are crucial for various purposes, including water, hazard, and agricultural management. Climate has an impact on vegetation, however, studying their relationship is challenging. We implemented the Least-Squares Wavelet (LSWAVE) software for investigating trend, coherency, and time lag estimation between climate and vegetation time series. We utilized Normalized Difference Vegetation Index (NDVI) time series provided by the Terra satellite and hybrid climate time series. We found that the seasonal cycles of climate and NDVI are coherent with time delay. For the entire Athabasca River Basin (ARB), the most coherent component was the annual cycle with 84% annual coherency between vegetation and temperature and 46% between vegetation and precipitation. The annual cycles of temperature and precipitation led the ones in vegetation by about two and three weeks, respectively. Relatively lower coherency was observed in the mountainous region (upper ARB) and higher coherency in the middle ARB. From the cross-spectrograms, a clear time delay pattern was observed between the annual cycles of climate and vegetation since 2000 but not for other high-frequency seasonal cycles. The results also highlighted the advantages of LSWAVE algorithms over traditional algorithms, such as linear regression and correlation. Furthermore, we analyzed the annual land use and land cover data provided by the Terra and Aqua satellites and discussed their linkage with the climate and NDVI results.

1. Introduction

Climate change has a significant influence on vegetation and water resources in river basins across the world. Vegetation plays a crucial role in carbon cycle regulation, water balance, human life, wildlife, etc. (Ghorbanian et al., 2022; Ren et al., 2022; Sun et al., 2022). Understanding how climate and vegetation interact with each other both spatially and temporally across river basins can help agronomists, policymakers, and other responsible authorities for proper management and decision-making. As the intensity of sunlight varies during each year due to the tilted Earth's spin axis, seasonal cycles are often observed in climate, and vegetation within watersheds. The interaction

between changes in climate and vegetation is not however straightforward. Depending on soil characteristics, type of land cover, anthropogenic activities, and other factors, this interaction can be highly complex. For example, there can be a time delay between seasonal cycles of temperature, precipitation, and vegetation. This study investigates the relationship between climate and vegetation/land cover in both time and space for the Athabasca River Basin (ARB) in Alberta, Canada.

The adaptations of Land Use/Land Cover (LULC) have raised concerns due to its position in diminishing the variety of life, altering local climate, and instituting an Urban Heat Island (UHI) in cities (Ullah et al., 2019; Camilleri et al., 2017). The biophysical characteristics

* Corresponding author.

E-mail addresses: hatef.dastour@ucalgary.ca (H. Dastour), ebrahim.ghaderpour@uniroma1.it (E. Ghaderpour), mohamed.abdelsamie@ucalgary.ca (M.S. Zaghloul), babak.farjad@gov.ab.ca (B. Farjad), anil.gupta@gov.ab.ca (A. Gupta), hyung.eum@gov.ab.ca (H. Eum), gachari@ucalgary.ca (G. Achari), qhassan@ucalgary.ca (Q.K. Hassan).

¹ Authors contributed equally to the manuscript.

² This research was conducted when Ebrahim Ghaderpour was affiliated with Department of Geomatics Engineering, University of Calgary, 2500 University Drive NW, Calgary, AB T2N 1N4, Canada.

<https://doi.org/10.1016/j.jag.2022.103044>

Received 1 July 2022; Received in revised form 21 September 2022; Accepted 29 September 2022

Available online 21 October 2022

1569-8432/© 2022 The Author(s). Published by Elsevier B.V. This is an open access article under the CC BY license (<http://creativecommons.org/licenses/by/4.0/>).

of the surface of the land are known as land cover, whereas how humans use a certain land is known as land use (Ullah et al., 2019). Due to interconnectivity between land cover and land use, these two are frequently studied together (Verburg et al., 2009). Furthermore, analyzing climate and vegetation with their possible relationships can provide an excellent resource for better resource management and planning (Usman et al., 2015; Talukdar et al., 2020).

Since the 1970s, changes in LULC and increases in agriculture/food production have been affecting climatic changes to a greater extent in the wake of the release of a disproportionate amount of greenhouse gases into the atmosphere (Rahaman and Hassan, 2017). There has been a number of studies that analyzed the relationship between climate change and LULC changes (Hassan and Rahman, 2013; Rahaman and Hassan, 2017). Perugini et al. (2017) investigated the relationship between changes in surface air temperature, precipitation, and land cover changes. They indicated that large-scale (extreme) land cover changes may have a robust regional effect on temperature and precipitation, and a significant global impact on temperature. Tran et al. (2017) indicated that the association between Land Surface Temperature (LST) and each LULC could be nonlinear because there may exist dissimilarity between each LULC type, and it could be connected to the geographical setting and season. Hassan and Rahman (2013) illustrated the prospect of MODIS-based Accumulated Growing Degree Days (AGDD) in determining the phenological stage of Deciduous Leaf Out (DLO) over the boreal-forested areas in Alberta. They found that the DLO can be determined with reasonable agreements for the majority of the cases (91.9%).

There are many indices developed for LULC mapping and analysis. For instance, Normalized Difference Vegetation Index (NDVI) (Petreoli et al., 2005), Enhanced Vegetation Index (EVI) (Ghaderpour and Vujadinovic, 2020b), Normalized Difference Built-Up Index (NDBI) (Zha et al., 2003), and an Index-based Built-up Index (IBI), Xu (2008), and Soil-Adjusted Vegetation Index (SAVI) (Huete, 1988). The NDVI is a compelling index for monitoring vegetation, soil, water, etc. (Hassan and Bourque, 2010; Rahaman et al., 2018), and it provides consistent spatial and temporal comparisons of vegetation canopy greenness, a composite property of leaf area, chlorophyll, and canopy structure (Walker et al., 2003; Ghaderpour et al., 2020). Extreme events, such as droughts, floods, fires, insect attacks, urbanization, etc., can result in rapid changes in the NDVI time series. Other studies also discussed the relationship between LULC, NDVI, and LST (Lu and Weng, 2006; She et al., 2015; Hassan et al., 2021).

Remote sensing time series are often irregularly sampled due to several reasons, including cloud contamination, sensor defects, economy, and storage issues (Aredhehy et al., 2018; Xu et al., 2019; Ghaderpour and Vujadinovic, 2020a). There are several methods developed for reconstructing time-series NDVI images. For instance, one of the methods that are increasingly being employed for reconstructing time series of NDVI is Harmonic Analysis of Time Series (HANTS) (Jia et al., 2011; Zhou et al., 2015; Aredhehy et al., 2018). However, the Least-Squares Wavelet (LSWAVE), developed by Ghaderpour and Pagiatakis (2019), does not require any forms of preprocessing and gap-filling. The LSWAVE contains several tools, such as Least-Squares Cross-Wavelet Analysis (LSCWA) and Anti-Leakage Least-Squares Spectral Analysis (ALLSSA) (Vaníček, 1969; Ghaderpour and Vujadinovic, 2020c; Ghaderpour et al., 2021b). The ALLSSA pinpoints an optimal series of functions (e.g., sinusoids and trends) and fits concurrently to the time series which can prevent over/under-fitting problems (Ghaderpour et al., 2021b). One of the advantages of LSCWA is that it does not mandate regularly sampled time intervals. Thus, there is no need for aggregating the time series data that can create biases (Ghaderpour and Pagiatakis, 2017; Ghaderpour et al., 2018a, 2021b).

Since the blooming of the oil and gas industry in 1967, the ARB has been playing a pivotal role in the economy of Alberta. Some of the other major activities in this region are forestry, agriculture, tourism, coal, and oil sand mining (Afrin et al., 2019). The majority of the ARB

land cover type is the boreal forest (82% of the total land) (Meshesha et al., 2021). Boreal forest in the ARB provides livelihood to more than 150,000 residents with 13% of indigenous people living there, and it influences the culturally vibrant and diversity of Alberta (Papaioannou et al., 2010; Afrin et al., 2019). Owing to urbanization and industrial activities including coal and oil sand mining, natural gas extraction, agricultural expansion, forest degradation, and pulp and paper production, the ARB has changed rapidly in the last few decades. Other than these man-made activities, natural hazards such as wildfire also transformed the landscape of the basin (Papaioannou et al., 2010; Afrin et al., 2019; Meshesha et al., 2021).

Our main goal in this study was to investigate the association between climate (i.e. temperature and precipitation) and vegetation for three ARB subregions, namely, upper (southern mountainous region), middle, and lower (northern near the Lake Athabasca). To do so, we analyzed 16-day MODIS-NDVI (500 m) and Hybrid Climate Data (10 km) as well as annual MODIS-LULC (500 m). Ghaderpour et al. (2021b) successfully applied the LSWAVE software to investigate a possible relationship between climate and NDVI across ARB in the time–frequency domain. In this study, we also utilized the LSWAVE software to explore the possible influence of climate change on vegetation, and we employed the LSCWA for coherency and identifying phase differences between NDVI and temperature/precipitation. To our best knowledge, this was the first attempt for exploring the time–frequency analysis of climate and vegetation in the ARB. The finding of this research is paramount as it exhibits how temperature and precipitation variations may contribute to defining the inter- and intra-annual components (seasonal) of the NDVI time series. To summarize this, the main contributions of this research are listed below:

- Estimation of trends and correlation between the climate and vegetation time series in ARB and its three subregions.
- Estimation of coherency and time delay between seasonal cycles of climate and vegetation in ARB and its three subregions using the tools in LSWAVE software.
- Discuss the potential linkage between LULC and the coherency results and highlight additional information that one can obtain when performing time–frequency analysis.

2. Materials and methods

2.1. Study region

The ARB covers about 24% of Alberta, and it is approximately 160,000 square km (Shrestha and Wang, 2018). It comprises 94 rivers, 153 lakes, 150 titled creeks, and many untitled creeks. The ARB exhibits wider variations in climatic, landscape, and topographic configurations. Seasonal climate conditions may impact river flow regimes. The ARB climate includes both cold and warm seasons. During its cold season, snow is the most dominant component of the precipitation, and during its warm season, glacial and snow from the headwaters of the rivers merge with the resultant runoff driven by local rainfall and snowmelt events. Water from each sub-basins also contributes to the river as it discharges into Lake Athabasca. In terms of land use, most of the ARB is forested and agricultural land (82% and 9.5%, respectively) (Shrestha et al., 2017; Ghaderpour et al., 2021b; Meshesha et al., 2021).

Fig. 1 exhibits the ARB region with a Digital Elevation Model (DEM) background layer acquired from Shuttle Radar Topography Mission (SRTM) at 30 m spatial resolution. The ARB region is divided into three subregions lower, middle, and upper (The Regional Aquatics Monitoring Program (RAMP), 2022). The borders of the province of Alberta (AB) are shown by a solid black line.

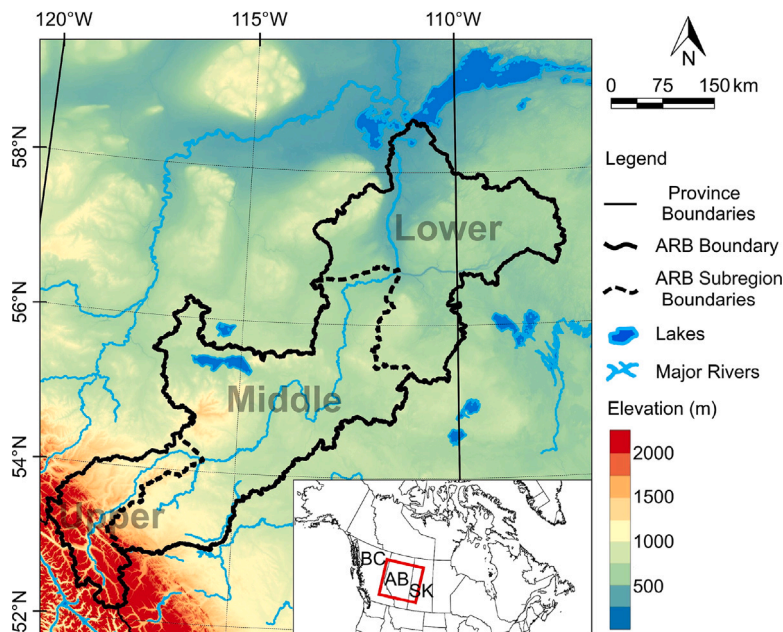


Fig. 1. Map of the ARB and surrounding watersheds, where Digital Elevation Model (DEM) at 30 m obtained from Shuttle Radar Topography Mission (SRTM) as a backdrop.

2.2. Data sets and pre-processing

In this study, we used historical climate data that comprises daily-maximum and daily-minimum temperatures and daily precipitation, for a span of twenty-year (2000–2019). Eum and Gupta (2019) proposed the REFERENCE Reliability Evaluation System (REFRES) which generates a high-resolution (0.1×0.1 degree—approximately 10 km) hybrid climate dataset through mathematically ranking multiple climate datasets. The authors also pointed out that the climate data were less reliable at the high altitude (the southwest of the ARB). It might be due to topographic variations, orographic repercussions, and limited ground data (Eum and Gupta, 2019). The present dataset is available for 1950–2019, provided by the Alberta Environment and Parks.

We employed Moderate Resolution Imaging Spectroradiometer (MODIS) NDVI, MOD13A1 (V006), and MODIS Land Cover Type 3 (LULC), MCD12Q1 (V006), for vegetation monitoring. All imagery was downloaded from the Google Earth Engine (GEE) (Gorelick et al., 2017). The NDVI imagery was available for a span of 20 years between early 2000 to the end of 2019, and MODIS annual LULC was available since 2001, excluding 2000. In this study, we used 16-day MODIS-NDVI imagery at 500 m spatial resolution and the annual MODIS Land Cover Type 3 (LULC) at 500 m resolution (Sulla-Menashe and Friedl, 2018). Using the pixel quality band provided with the MODIS data product, the cloudy pixels were masked out.

2.3. Methods

2.3.1. Spatial analysis

The climate data used in this study has a spatial resolution of 0.1 degrees (~ 10 km) in both latitude and longitude. For each spatial grid, the daily average temperature was calculated based on the daily minimum and maximum temperatures. Using these average temperature data, first, the means of average temperature for all spatial grids and each month were calculated for the entire period. Then, the mean of these monthly average temperatures was calculated for each month. Similarly, using daily precipitation data, first, total precipitation was calculated for each month, and each spatial grid, and then, the mean of these total precipitations was calculated for each month as monthly total precipitation averaged over 2000–2019.

Moreover, using MODIS-NDVI 500 m data from 2000–2019, monthly NDVI values were calculated for each month. For example,

to calculate monthly MODIS-NDVI averaged over 2000–2019 for January, first, the mean NDVI values for each January from the period were calculated, and then these calculated values were averaged for each pixel. Additionally, a similar approach as above was utilized for calculating annual average temperature, annual total precipitation, and annual MODIS-NDVI values averaged over 2000–2019.

2.3.2. Trend analysis

Pearson correlation is one of the most common metrics used in statistics that shows the strength and direction of a linear relationship between two variables (Lee Rodgers and Nicewander, 1988). This metric is shown by r .

The average NDVI value for each image from the 16-day MODIS-NDVI (500 m) dataset was calculated for the ARB subregions and the entire ARB. The average temperature corresponding to the time window associated with each NDVI was calculated for each subregion and the entire ARB. Similarly, accumulated precipitation (the summation of average precipitation for each day) was calculated for all subregions. Pearson correlation between NDVI and average-temperature/precipitation values was calculated by the ARB subregion.

Least-Squares Spectral Analysis (LSSA) can fit the sinusoidal function family to the entire time series without any requirement for pre-processing (Craymer, 1998; Pagiatakis, 1999; Ghaderpour et al., 2021b). In this article, we used an iterative procedure established on the LSSA which likewise fits the sinusoidal function family to the entire time series (Ghaderpour et al., 2018b, 2021b). Especially, when a time series is irregularly sampled (unequally spaced), ALLSSA can perform better than LSSA in terms of the accuracy of signal estimation (Ghaderpour et al., 2018b, 2021b). In addition to the traditional linear fit, ALLSSA was implemented for performing season-trend analyses on the same dataset which was used for calculating Pearson correlations. The ALLSSA equation is

$$y = c_1 + c_2 t + \sum_{i=1}^m (a_i \cos(2\pi\omega_i t) + b_i \sin(2\pi\omega_i t)) \quad (1)$$

where t is the observed values, m is an optimal number of harmonics to be determined, and coefficients c_1 , c_2 , a_i , b_i , ω_i are estimated iteratively at a 99% confidence level threshold. This is a threshold in the spectral domain where the harmonics are interactively estimated.

2.3.3. Coherency analysis

For two given time series, phase discrepancies or time delays between inter- and intra-annual cycles of two time series can be estimated. For the seasonal components of two time series, coherency analysis assesses the time lags, and it can exhibit the coherency of components in the time–frequency (or just frequency) domain (Ghaderpour et al., 2021b, 2018a). Ghaderpour et al. (2018a) proposed the LSCWA for coherency investigation and assessment of phase discrepancies between the spectral features of two time series. For two time series, LSCWA reproduces the least-squares wavelet spectrograms of the series and provides the phase differences in the time–frequency domain like the cross-wavelet transform (XWT) (Torrence and Compo, 1998). Some of the advantages of LSCWA over XWT can be discussed as follows. First, LSCWA does not require regularly sampled time intervals; thus, there is no need for data aggregation (Ghaderpour and Vujadinovic, 2020b; Ghaderpour et al., 2021b). Furthermore, the cross-wavelet spectrogram in LSCWA has a higher time–frequency resolution in contrast to XWT (Ghaderpour et al., 2021b). The spectrograms are generated through translating windows over time for each frequency where the size of each window is contrariwise related to the frequency. Within each window, the sinusoidal functions will be fitted to the time series segment to estimate the least-squares spectral peaks corresponding to each time and frequency. Gaussian weights may also be used during the fitting process to give more weight to the time series values close to the window center and less weight toward the window margins as the window translates. This will acclimate the sinusoidal function family to the Morlet wavelet through least-squares and optimize the time–frequency resolution of the spectral peaks (Ghaderpour et al., 2021a).

The individual time series-specific lags/leads of components can be discerned from the phase-shifting associated with the cross-spectrogram's spectral peaks. The phase-shifting is usually portrayed by arrows on the substantial spectral peaks in the cross-spectrogram as per the two-dimensional Cartesian coordinate system's trigonometric circle principle (Ghaderpour et al., 2018a). For two time series, within the windows where they were assessed, arrows fronting the positive/negative time-axis signify the seasonal components of the second time series are in-phase/out-of-phase in comparison to those of the first time series. Similarly, arrows fronting the positive/negative frequency-axis illustrate the seasonal components of the second time series are lagging/leading in comparison to those of the first time series (Ghaderpour and Vujadinovic, 2020c). Fig. 2 demonstrates a schematic graph for phase arrows in LSCWA. As a case in point, the red and blue signals can depict the annual cycles in temperature and vegetation.

The dataset from Section 2.3.2 was utilized here as well. For corresponding seasonal components of two time series, the coherency, here, is denoted by a percentage variance. The closer this percentage variance is to 100%, the more coherent the two time series are. We considered spectral peaks in the cross-spectrograms statistically significant if they meet a least a 99% confidence level threshold (Ghaderpour et al., 2018a). The Least-Squares Cross-Spectral Analysis (LSCSA) is a frequency domain algorithm based on LSCWA that estimates phase shifting and coherency only (unlike LSCWA which also includes time-domain assessments) (Ghaderpour and Vujadinovic, 2020c).

2.3.4. Land cover variation

We used the LULC dataset based on Leaf Area Index (LAI) classes from Sulla-Menashé and Friedl (2018) for our land cover analysis. Land cover classes available in our LULC dataset for the ARB are Grasslands, Water Bodies, Shrublands, Savannas, Deciduous Broadleaf Forests, Urban and Built-up Lands (in this article, we refer to this class as Urban), and Deciduous Needleleaf Forests, Evergreen Needleleaf Forests, Non-Vegetated Lands. The observation percentage of each class was calculated for each year, and then the average of these percentages was calculated for the period 2000–2019. We also estimated the linear trends by each LULC type. As there was no seasonality in these values, the simple fit was adequate for this trend estimation.

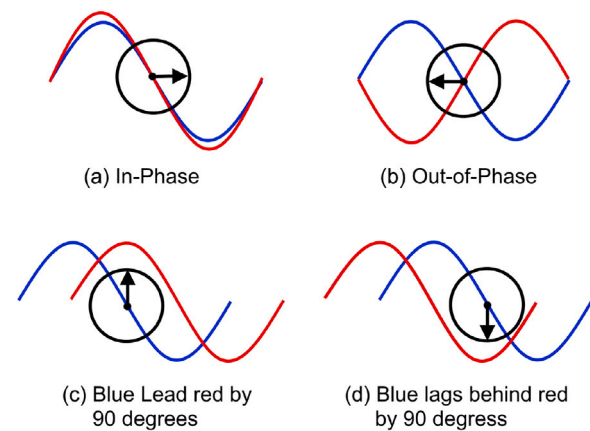


Fig. 2. A schematic diagram for phase arrows in LSCWA. As an example, the red and blue signals may represent the annual cycles in temperature and vegetation. (For interpretation of the references to color in this figure legend, the reader is referred to the web version of this article.)

3. Results

As described earlier, MODIS-NDVI, LULC, and climate data were used for performing various analyses. In this section, the results of remote sensing spatial variation, climate trend analysis, coherency, time-delay analyses, and MODIS land cover variation are demonstrated.

3.1. Remote sensing spatial variation

Fig. A.3 demonstrates monthly MODIS-NDVI values for the ARB region, averaged over 2000–2019. As can be seen, overall, July and August had the highest mean NDVI values, and December to March had the lowest mean NDVI values. The southwest part of the upper ARB had the lowest mean NDVI values, while the middle ARB had the highest mean NDVI values overall. Fig. A.4 highlights monthly average temperature values, averaged over 2000–2019, for the ARB region. Fig. A.4 also shows that July and August had the highest average temperature, while December and January had the lowest average temperature. It also can be seen that the northeastern part of the lower ARB had the lowest average temperature values during the coldest months and the highest temperatures during the warmest months. During December, January, and February, lower average temperatures are owing to short winter days and Arctic frontal. This is a regular continental regime (Downing and Pettapiece, 2006; Rahaman and Hassan, 2017). The monthly total precipitation values for the ARB region, averaged over 2000–2019, are illustrated in Fig. A.5. Note that the total precipitation had its maximum value in June and July. Finally, annual MODIS-NDVI map (Fig. 3a), annual average temperature (Fig. 3b), and annual total precipitation map (Fig. 3c) averaged over 2000–2019 are illustrated in Fig. 3.

3.2. Climate trend analysis

In Fig. A.1, Pearson correlation was utilized to demonstrate the strength and direction of a linear relationship between average temperature and NDVI values for three subregions of the ARB. As can be seen, the correlation between average temperature and MODIS-NDVI values was relatively high (the lowest was 0.88 and the highest was 0.92) for all subregions of the ARB. Similarly, the Pearson correlation was also used for the precipitation and MODIS-NDVI values for all subregions of the ARB. The correlation between precipitation and NDVI values was much less than those between average temperature and NDVI (the lowest correlation was 0.34 and the highest correlation was 0.64). For

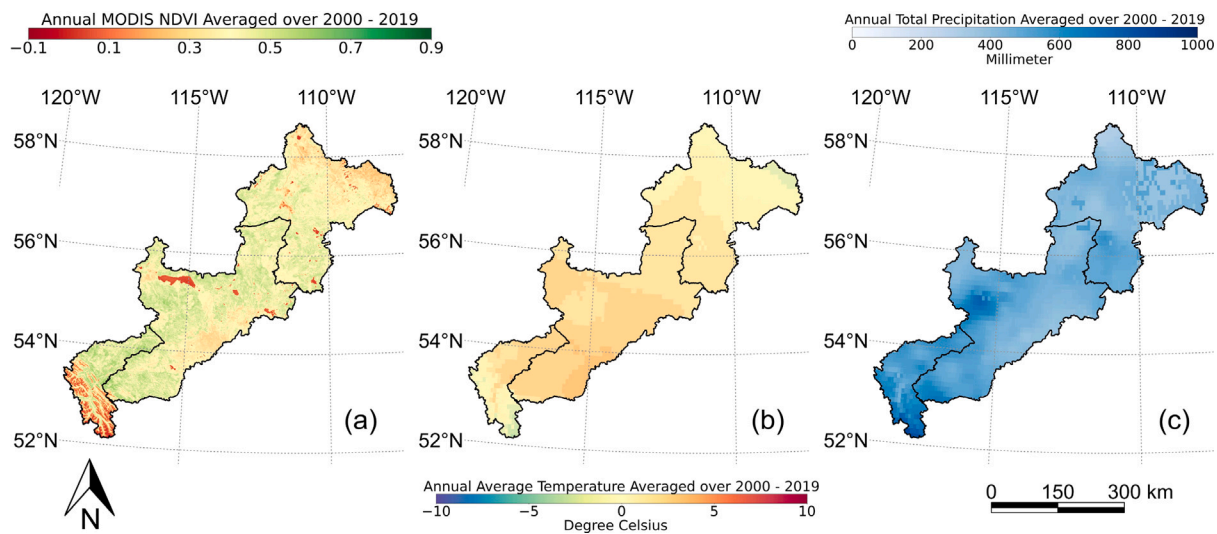


Fig. 3. Annual MODIS-NDVI (a), annual average temperature (b), and annual total precipitation (c) averaged over 2000–2019. (For interpretation of the references to color in this figure legend, the reader is referred to the web version of this article.)

Table 1

The ALLSSA season-trend fit estimates at 99% confidence level for temperature and precipitation time series corresponding to ARB and its subregions.

Average temperature (°C)					
ARB Subregion	Intercept (°C)	Slope (°C/yr)	Amplitude (°C)		
			At frequency 1 cycle/yr	At frequency 2 cycles/yr	At frequency 3 cycles/yr
Full	1.283 ± 0.330	−0.004 ± 0.028	15.325 ± 0.231		
Lower	0.326 ± 0.359	0.002 ± 0.031	17.523 ± 0.252	0.786 ± 0.251	
Middle	2.051 ± 0.334	0.001 ± 0.029	14.498 ± 0.234		
Upper	1.313 ± 0.293	−0.041 ± 0.026	11.500 ± 0.208	0.899 ± 0.207	0.406 ± 0.207
Precipitation (mm)					
ARB Subregion	Intercept (mm)	Slope (mm/yr)	Amplitude (mm)		
			At frequency 1 cycle/yr	At frequency 2 cycles/yr	At frequency 3 cycles/yr
Full	20.655 ± 1.006	0.084 ± 0.087	16.896 ± 0.705	7.758 ± 0.704	2.856 ± 0.703
Lower	19.927 ± 1.172	−0.033 ± 0.101	15.973 ± 0.821	7.657 ± 0.820	2.661 ± 0.819
Middle	20.233 ± 1.234	0.160 ± 0.106	18.201 ± 0.864	8.524 ± 0.862	3.158 ± 0.861
Upper	24.797 ± 1.479	0.160 ± 0.129	15.270 ± 1.050	5.792 ± 1.047	3.333 ± 1.046

upper ARB in particular (Fig. A.1e and Fig. A.1f), the correlations are lower than in the rest of the ARB subregions.

In Fig. A.2, simultaneous season-trend (dashed blue line) fit models are available. From Table 1, in terms of average temperature, the slope (ALLSSA) of the average temperature for the upper ARB region was −0.041 °C/year, and the overall trend for the average temperature of the upper ARB was negligibly decreasing. The slopes (ALLSSA) of precipitation were 0.160 mm/year for both middle and upper ARB. It is evident that the overall trend for precipitation in these subregions was narrowly increasing.

3.3. Coherency and time-delay analyses

Fig. 4 shows the coherency analysis between MODIS-NDVI (500 m) and Climate for the Full ARB since 2000. Note that in the middle panels, the annual cycle of the precipitation leads the annual cycle of NDVI by about 3 weeks, and the annual cycle of the temperature leads the annual cycle of NDVI by about 2 weeks on average. The bottom panels are the coherency results when the annual cycle is removed. The semi-annual components (2 cycles/year) of climate generally lead the semi-annual component of NDVI. The direction of the arrows on the annual peaks in the cross-spectrogram indicates that when the temperature and precipitation reach their annual maximum values, the NDVI reaches its annual maximum only a few weeks later. Likewise, the NDVI reaches its annual minimum a few weeks after the temperature and precipitation reach their annual minimum. In other words, the

Table 2

The coherency and phase results between NDVI and climate for the ARB subregions.

Annual cycle (1 cycle/year)	Upper ARB	Middle ARB	Lower ARB	Full ARB
NDVI-Precipitation	26%	41%	38%	46%
Precipitation leads NDVI by	4 weeks	3 weeks	2 weeks	3 weeks
NDVI-Temperature	73%	82%	83%	84%
Temperature leads NDVI by	3 weeks	2 weeks	2 weeks	2 weeks

annual cycles of climate and vegetation are coherent but with a phase delay. There is a similar discussion for other coherent seasonal cycles as observed in the residual cross-spectrograms. The overall (twenty-year) coherency and phase results for the annual components of NDVI and climate for the ARB regions are listed in Table 2. Note that the results listed in Table 2 are not based on LSCWA which is in the time-frequency domain but based on LSCSA which is only in the frequency domain. That may “loosely” be viewed as the average of the directions of all the arrows displayed on the annual peaks in the LSCWS. The LSCWA results for lower, middle, and upper ARB are very similar and omitted here for brevity.

3.4. Land cover variation

Annual MODIS land cover data at 500 m spatial resolution were analyzed to generate Fig. 5. Fig. 5 displays the spatial variation of MODIS-LULC for the years 2001, 2010, and 2019 (nine years apart).

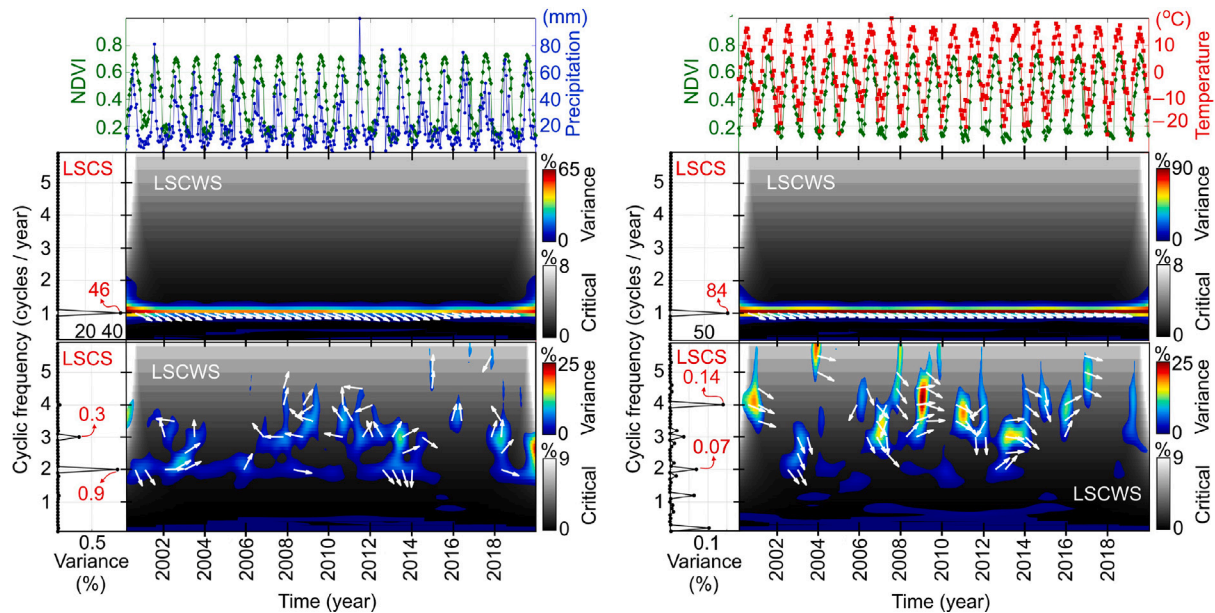


Fig. 4. Phase differences and coherency analysis for the entire ARB. The gray background demonstrates the dynamic surface with a confidence level of 99%. White arrows pointing to east, west, south, and north mean in-phase, out-of-phase, climate leads, and NDVI leads, respectively.

Savannas, Evergreen Needleleaf Forests, and Grasslands cover the abundance of the ARB. The temporal dynamic variations of land cover type and their corresponding trendlines within each ARB subregion are exhibited in Fig. A.6. The estimated LULC types trend coefficients with their respective p-values for three subregions of ARB and the entire ARB are available in Table A.1. From Fig. A.6(a) and Fig. A.6(e), it can be observed that the majority of the lower ARB, just above 70%, was covered by Savannas during the period of interest while nearly 17% of the subregion was covered by Evergreen Needleleaf Forests. From A.6 (b) can be seen that these Savannas and Evergreen Needleleaf Forests contributed more equally to the land coverage of the middle ARB, especially from 2015–2019. From Fig. A.6(c), over 40% of the upper ARB was covered by Evergreen Needleleaf Forests during the period of interest. Fig. A.6(d) shows that Savannas were responsible for nearly 50%, on average, of the entire ARB area coverage while on average, just under 30% of the entire ARB was covered by Evergreen Needleleaf Forests. According to the MODIS-LULC, Broadleaf Croplands and Evergreen Broadleaf Forests had zero presence in the ARB region during the period of interest. Seven MODIS land cover classes are illustrated in Fig. A.6(e) as, during 2000–2019, Broadleaf Croplands and Evergreen Broadleaf Forests had zero area coverage, and Urban had an insignificant area coverage, 0.04%, 0.07%, 0.07%, 0.06% for the lower, middle, upper, and entire ARB, respectively.

Pearson correlation was also used for identifying the relationship between the coverage area of various LULC classes. Fig. A.7 highlights this Pearson correlation table for all three subregions of the ARB and the entire ARB. From Fig. A.6(b) and Table A.1, one can observe that in the middle ARB, the coverage percentage of Evergreen Needle Forests was increasing slightly (with a slope of 0.432) while the coverage percentage of Savannas was decreasing narrowly. On the other hand, as Fig. A.7(b) demonstrates, the correlation between these two types was -0.98 which highlights the inverse relationship between these two LULC types.

4. Discussion

In this research, correlation and coherency between climate and NDVI time series were investigated for ARB and its subregions (Fig. A.1, Fig. 4, Table 2). The Pearson correlations, least-squares cross-spectral, and cross-wavelet analyses were performed on subregions of

ARB that are relatively homogeneous subregions in terms of land cover, soil, topography, climate, ecology, etc. The Pearson correlations only provided possible linear dependency between climate and NDVI, while LSCSA and LSCWA showed how climate and NDVI time series are coherent in frequency and time-frequency domains, respectively, and how much their inter- and intra-annual cycles lag or lead from each other.

From Table 2, Fig. 5 and Fig. A.6, it is apparent that the upper ARB is a mountainous area and had noticeably more non-vegetated area coverage (almost 8.5%) as compared to those of the middle and lower ARB, 0.02% and 0.29%, respectively. This may explain a lower amount of coherency between NDVI and temperature 73% for upper ARB in comparison to those of middle ARB and lower ARB, 82% and 83%, respectively, and similarly, a lower correlation between NDVI and the average temperature in the upper ARB. Note that the low NDVI values observed in the mountainous part of upper ARB are due to several factors, such as snow/ice, water, soil, and possible cloud effects which may have remained after the cloud masking, see reddish colors in Fig. 3 and Fig. A.3. Additionally, with respect to vegetation and precipitation, likewise, middle ARB and lower ARB had more vegetation coverage than upper ARB, which may explain why coherency between NDVI and precipitation was higher in middle ARB (41%) and lower ARB (38%) in comparison to that of upper ARB (26%). A slight increase in precipitation in the middle ARB (see 1.60 ± 0.106 mm/year in Table 1) was likely one of the contributors to the area coverage increase for Evergreen Needle Forests. From Fig. A.6(d) and Table A.1, it can be observed that during the period 2000–2019, in the lower and upper ARB which Savannas had more presence and Evergreen Needle Forests had less presence. From Fig. A.7(b) and (c), the negative correlations between these two LULC types also reiterate that there was an inverse relationship between these two LULC types during the period of interest.

Some of the constraints of this study are listed below. Despite the cloud masking, satellite imagery may still be contaminated by clouds, cloud shadows, haze, smoke, etc. Therefore, the NDVI values have uncertainties (Ghaderpour and Vujadinovic, 2020a; Xu et al., 2019). For MODIS Land Cover (MCD12Q1) product, wetlands can be under-represented, and some grassland areas can be classified as savannas (sparse forest) (Sulla-Menashe and Friedl, 2018).

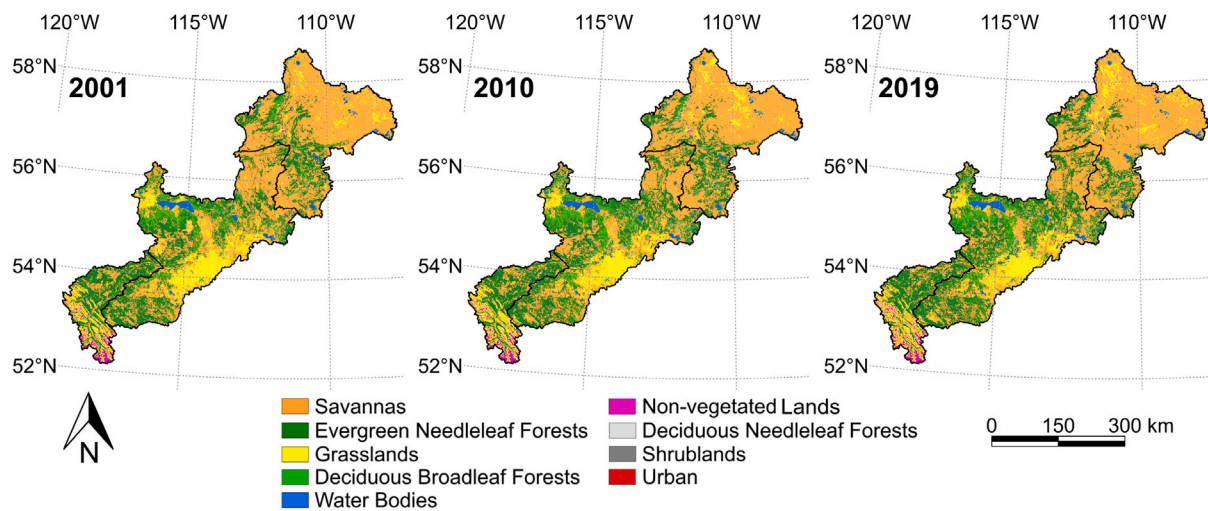


Fig. 5. MODIS land cover classes dynamics for 2001, 2010, and 2019.

5. Conclusion

In this paper, spatiotemporal interactions between NDVI, climate, and LULC for ARB were investigated using the LSWAVE software and also through various geospatial mapping techniques. The ALLSSA showed that the overall trend for precipitation was increasing slightly for the upper and middle ARB subregions since 2000, and the overall trend for the average temperature of upper ARB was slightly decreasing (approximately 0.8 °C declined since 2000). Overall, monthly NDVI values averaged over 2000–2019 had their highest values during July and August and their lowest values from December to March. Moreover, July and August had the highest monthly average temperature, while December and January had the lowest monthly average temperature. In addition, monthly total precipitation values averaged over 2000–2019 had their highest value in June and July. As it appears, NDVI met its highest/lowest values when temperature and precipitation also met their highest/lowest values approximately. However, the temporal influence of climate on vegetation was not clear from spatial maps. Therefore, we went one step deeper and for each subregion of the ARB that has its own characteristics in terms of topography, climate, soil, etc. we performed coherency and phase delay analyses. The majority of the ARB subregions were covered with savannas (sparse forest), evergreen needleleaf forests, and grasslands during the period of interest with an insignificant change since 2001. Both LSCWA and LSCSA showed that the annual cycles of the climate and NDVI time series are significantly coherent at 99% confidence level. Upper ARB showed less coherency between NDVI and the average temperature in comparison to those of middle and lower ARB due to lower vegetation coverage. Similarly, for upper ARB, the coherency between NDVI and precipitation was also lower than those of lower and middle ARB for the same reason. Additionally, the annual cycles of the precipitation and temperature were found to be leading the annual cycle of NDVI by about 3 and 2 weeks on average, respectively. Such results could not be deduced from the traditional analysis (e.g., Pearson correlation), highlighting LSWAVE software's potential applications.

CRedit authorship contribution statement

Hatef Dastour: Conceptualization, Formal analysis, Methodology, Writing—original draft. **Ebrahim Ghaderpour:** Conceptualization, Formal analysis, Methodology, Writing—original draft. **Mohamed Sherif Zaghloul:** Formal analysis, Methodology, Writing – review and editing. **Babak Farjad:** Methodology, Writing – review and editing. **Anil Gupta:** Methodology, Writing – review and editing. **Hyung Eum:** Methodology, Writing – review and editing. **Gopal Achari:** Methodology, Writing – review and editing. **Quazi K. Hassan:** Conceptualization, Methodology, Supervision, Writing – review and editing.

Declaration of competing interest

The authors declare that they have no known competing financial interests or personal relationships that could have appeared to influence the work reported in this paper.

Data availability

MODIS data is publicly available. The climate data also can be available from the Government of Alberta.

Acknowledgments

This research was funded by the Oil Sands Monitoring (OSM) Program of Alberta Environment and Parks (AEP), Canada. It was independent of any position of the OSM Program. OSM had no role in the study design, data collection and analysis, decision to publish, and preparation of the manuscript. Also, the authors would acknowledge the: (i) Government of Alberta (Alberta Agriculture and Forestry) for providing gridded climate data for non-commercial/research purposes free of cost, and (ii) USGS for providing the MODIS- NDVI imagery and MODIS Land Cover Type 3, while Google personnel for their excellent work on making these free data sets available on Google Earth Engine. All authors have read and agreed to the published version of the manuscript.

Appendix A. Supplementary data

Supplementary material related to this article can be found online at <https://doi.org/10.1016/j.jag.2022.103044>.

References

- Afrin, S., Gupta, A., Farjad, B., Ahmed, M.R., Achari, G., Hassan, Q.K., 2019. Development of land-use/land-cover maps using Landsat-8 and MODIS data, and their integration for hydro-ecological applications. *Sensors* 19 (22), 4891.
- Aredehey, G., Mezgebu, A., Girma, A., 2018. Land-use land-cover classification analysis of Giba catchment using hyper temporal MODIS NDVI satellite images. *Int. J. Remote Sens.* 39 (3), 810–821.
- Camilleri, S., De Giglio, M., Stecchi, F., Pérez-Hurtado, A., 2017. Land use and land cover change analysis in predominantly man-made coastal wetlands: towards a methodological framework. *Wetl. Ecol. Manag.* 25 (1), 23–43.
- Craymer, M.R., 1998. *The Least Squares Spectrum, Its Inverse Transform and Autocorrelation Function: Theory and Some Applications in Geodesy*. University of Toronto.
- Downing, D., Pettapiece, W., 2006. *Natural Regions and Subregions of Alberta*. Natural Regions Committee: Government of Alberta, Alberta, Canada.

- Eum, H.-I., Gupta, A., 2019. Hybrid climate datasets from a climate data evaluation system and their impacts on hydrologic simulations for the Athabasca river basin in Canada. *Hydrol. Earth Syst. Sci.* 23 (12), 5151–5173.
- Ghaderpour, E., Ben Abbes, A., Rhif, M., Pagiatakis, S.D., Farah, I.R., 2020. Non-stationary and unequally spaced NDVI time series analyses by the LSWAVE software. *Int. J. Remote Sens.* 41 (6), 2374–2390.
- Ghaderpour, E., Ince, E.S., Pagiatakis, S.D., 2018a. Least-squares cross-wavelet analysis and its applications in geophysical time series. *J. Geod.* 92 (10), 1223–1236.
- Ghaderpour, E., Liao, W., Lamoureux, M.P., 2018b. Antileakage least-squares spectral analysis for seismic data regularization and random noise attenuation. *Geophysics* 83 (3), V157–V170.
- Ghaderpour, E., Pagiatakis, S.D., 2017. Least-squares wavelet analysis of unequally spaced and non-stationary time series and its applications. *Math. Geosci.* 49 (7), 819–844.
- Ghaderpour, E., Pagiatakis, S.D., 2019. LSWAVE: A MATLAB software for the least-squares wavelet and cross-wavelet analyses. *GPS Solut.* 23 (2), 1–8.
- Ghaderpour, E., Pagiatakis, S.D., Hassan, Q.K., 2021a. A survey on change detection and time series analysis with applications. *Appl. Sci.* 11 (13), 6141.
- Ghaderpour, E., Vujadinovic, T., 2020a. Change detection within remotely sensed satellite image time series via spectral analysis. *Remote Sens.* 12 (23), 4001.
- Ghaderpour, E., Vujadinovic, T., 2020b. The potential of the least-squares spectral and cross-wavelet analyses for near-real-time disturbance detection within unequally spaced satellite image time series. *Remote Sens.* 12 (15).
- Ghaderpour, E., Vujadinovic, T., 2020c. The potential of the least-squares spectral and cross-wavelet analyses for near-real-time disturbance detection within unequally spaced satellite image time series. *Remote Sens.* 12 (15), 2446.
- Ghaderpour, E., Vujadinovic, T., Hassan, Q.K., 2021b. Application of the least-squares wavelet software in hydrology: Athabasca river basin. *J. Hydrol.: Reg. Stud.* 36, 100847.
- Ghorbanian, A., Mohammadzadeh, A., Jamali, S., 2022. Linear and non-linear vegetation trend analysis throughout Iran using two decades of MODIS NDVI imagery. *Remote Sens.* 14 (15), 3683.
- Gorelick, N., Hancher, M., Dixon, M., Ilyushchenko, S., Thau, D., Moore, R., 2017. Google earth engine: Planetary-scale geospatial analysis for everyone. *Remote Sens. Environ.* 202, 18–27.
- Hassan, Q.K., Bourque, C.P.-A., 2010. Spatial enhancement of MODIS-based images of leaf area index: Application to the boreal forest region of northern Alberta, Canada. *Remote Sens.* 2 (1), 278–289.
- Hassan, Q.K., Ejiagha, I.R., Ahmed, M.R., Gupta, A., Rangelova, E., Dewan, A., 2021. Remote sensing of local warming trend in alberta, Canada during 2001–2020, and its relationship with large-scale atmospheric circulations. *Remote Sens.* 13 (17), 3441.
- Hassan, Q.K., Rahman, K.M., 2013. Applicability of remote sensing-based surface temperature regimes in determining deciduous phenology over boreal forest. *J. Plant Ecol.* 6 (1), 84–91.
- Huete, A.R., 1988. A soil-adjusted vegetation index (SAVI). *Remote Sens. Environ.* 25 (3), 295–309.
- Jia, L., Shang, H., Hu, G., Menenti, M., 2011. Phenological response of vegetation to upstream river flow in the Heihe river basin by time series analysis of MODIS data. *Hydrol. Earth Syst. Sci.* 15 (3), 1047–1064.
- Lee Rodgers, J., Nicewander, W.A., 1988. Thirteen ways to look at the correlation coefficient. *Amer. Statist.* 42 (1), 59–66.
- Lu, D., Weng, Q., 2006. Spectral mixture analysis of ASTER images for examining the relationship between urban thermal features and biophysical descriptors in Indianapolis, Indiana, USA. *Remote Sens. Environ.* 104 (2), 157–167.
- Meshesha, T.W., Wang, J., Melaku, N.D., McClain, C.N., 2021. Modelling groundwater quality of the Athabasca river basin in the subarctic region using a modified SWAT model. *Sci. Rep.* 11 (1), 1–12.
- Pagiatakis, S.D., 1999. Stochastic significance of peaks in the least-squares spectrum. *J. Geod.* 73 (2), 67–78.
- Papaioannou, A., Dovriki, E., Rigas, N., Plageras, P., Rigas, I., Kokkora, M., Papastergiou, P., 2010. Assessment and modelling of groundwater quality data by environmetric methods in the context of public health. *Water Resour. Manage.* 24 (12), 3257–3278.
- Perugini, L., Caporaso, L., Marconi, S., Cescatti, A., Quesada, B., de Noblet-Ducoudre, N., House, J.I., Arneth, A., 2017. Biophysical effects on temperature and precipitation due to land cover change. *Environ. Res. Lett.* 12 (5), 053002.
- Pettorelli, N., Vik, J.O., Mysterud, A., Gaillard, J.-M., Tucker, C.J., Stenseth, N.C., 2005. Using the satellite-derived NDVI to assess ecological responses to environmental change. *Trends Ecol. Evol.* 20 (9), 503–510.
- Rahaman, K.R., Ahmed, M.R., Hassan, Q.K., 2018. Using satellite-borne remote sensing data in generating local warming maps with enhanced resolution. *ISPRS Int. J. Geo-Inf.* 7 (10), 398.
- Rahaman, K.R., Hassan, Q.K., 2017. Quantification of local warming trend: A remote sensing-based approach. *PLOS ONE* 12 (1), 1–18.
- Ren, Y., Liu, J., Liu, S., Wang, Z., Liu, T., Shalamzari, M.J., 2022. Effects of climate change on vegetation growth in the Yellow River Basin from 2000 to 2019. *Remote Sens.* 14 (3), 687.
- She, X., Zhang, L., Cen, Y., Wu, T., Huang, C., Baig, M.H.A., 2015. Comparison of the continuity of vegetation indices derived from landsat 8 OLI and landsat 7 ETM+ data among different vegetation types. *Remote Sens.* 7 (10), 13485–13506.
- Shrestha, N.K., Du, X., Wang, J., 2017. Assessing climate change impacts on fresh water resources of the Athabasca river basin, Canada. *Sci. Total Environ.* 601, 425–440.
- Shrestha, N.K., Wang, J., 2018. Current and future hot-spots and hot-moments of nitrous oxide emission in a cold climate river basin. *Environ. Pollut.* 239, 648–660.
- Sulla-Menashe, D., Friedl, M.A., 2018. User Guide to Collection 6 MODIS Land Cover (MCD12Q1 and MCD12C1, Vol. 1) Product. USGS, Reston, VA, USA, p. 18.
- Sun, H., Chen, Y., Xiong, J., Ye, C., Yong, Z., Wang, Y., He, D., Xu, S., 2022. Relationships between climate change, phenology, edaphic factors, and net primary productivity across the Tibetan Plateau. *Int. J. Appl. Earth Obs. Geoinf.* 102708.
- Talukdar, S., Singha, P., Mahato, S., Pal, S., Liou, Y.-A., Rahman, A., et al., 2020. Land-use land-cover classification by machine learning classifiers for satellite observations—A review. *Remote Sens.* 12 (7), 1135.
- The Regional Aquatics Monitoring Program (RAMP), 2022. Overview of athabasca river basin landscape. [Online; accessed 01-March-2022].
- Torrence, C., Compo, G.P., 1998. A practical guide to wavelet analysis. *Bull. Am. Meteorol. Soc.* 79 (1), 61–78.
- Tran, D.X., Pla, F., Latorre-Carmona, P., Myint, S.W., Caetano, M., Kieu, H.V., 2017. Characterizing the relationship between land use land cover change and land surface temperature. *ISPRS J. Photogramm. Remote Sens.* 124, 119–132.
- Ullah, S., Tahir, A.A., Akbar, T.A., Hassan, Q.K., Dewan, A., Khan, A.J., Khan, M., 2019. Remote sensing-based quantification of the relationships between land use land cover changes and surface temperature over the lower himalayan region. *Sustainability* 11 (19), 5492.
- Usman, M., Liedl, R., Shahid, M., Abbas, A., 2015. Land use/land cover classification and its change detection using multi-temporal MODIS NDVI data. *J. Geogr. Sci.* 25 (12), 1479–1506.
- Vaníček, P., 1969. Approximate spectral analysis by least-squares fit. *Astrophys. Space Sci.* 4 (4), 387–391.
- Verburg, P.H., Van De Steeg, J., Veldkamp, A., Willemsen, L., 2009. From land cover change to land function dynamics: a major challenge to improve land characterization. *J. Environ. Manag.* 90 (3), 1327–1335.
- Walker, D., Epstein, H., Jia, G., Balser, A., Copass, C., Edwards, E., Gould, W., Hollingsworth, J., Knudson, J., Maier, H., et al., 2003. Phytomass, LAI, and NDVI in northern alaska: Relationships to summer warmth, soil pH, plant functional types, and extrapolation to the circumpolar arctic. *J. Geophys. Res.: Atmos.* 108 (D2).
- Xu, H., 2008. A new index for delineating built-up land features in satellite imagery. *Int. J. Remote Sens.* 29 (14), 4269–4276.
- Xu, X., Liu, H., Lin, Z., Jiao, F., Gong, H., 2019. Relationship of abrupt vegetation change to climate change and ecological engineering with multi-timescale analysis in the karst region, southwest China. *Remote Sens.* 11 (13), 1564.
- Zha, Y., Gao, J., Ni, S., 2003. Use of normalized difference built-up index in automatically mapping urban areas from TM imagery. *Int. J. Remote Sens.* 24 (3), 583–594.
- Zhou, J., Jia, L., Menenti, M., 2015. Reconstruction of global MODIS NDVI time series: Performance of harmonic analysis of time series (HANTS). *Remote Sens. Environ.* 163, 217–228.